This is the accepted version of:

Sreten Mastilovic, *Molecular-dynamics simulations of the nanoscale Taylor test under extreme loading conditions*. <u>Mathematics and Mechanics of Solids</u> **21** (3): 326-338, (2016). SAGE Publications.

Molecular-dynamics simulations of the nanoscale Taylor test under extreme loading conditions

Sreten Mastilovic
Union – Nikola Tesla University, Faculty of Construction Management, Serbia
E-mail: smastilovic@fgm.edu.rs

Abstract

A series of molecular-dynamics simulations of the classic Taylor impact test is performed by using a flat-ended monocrystalline nanoscale projectile made of the Lennard-Jones 2D solid. The nanoprojectile striking velocities range from 0.75 to 7 km/s. These atomistic simulations offer insight into nature of fragment distributions and evolution of state parameters. According to the simulation results, cumulative distribution of fragment sizes in the course of this non-homogeneous fragmentation process for hypervelocity impacts appears to be well represented by the bimodal-exponential distribution commonly observed during high-energy uniform fragmentation events. For more moderate impact velocities, the cumulative distribution of fragment sizes, in addition to the bimodal-exponential part, exhibits a large-fragment tail. Temporal evolutions on instantaneous kinetic temperature, stress and strain invariants are presented and discussed. Scaling relations between temperature/temperature rate and kinematic rates of deformation are suggested.

Keywords

Molecular dynamics, Taylor test, fragmentation, bimodal-exponential distribution, hypervelocity impact.

1. Introduction

The high-velocity impact of a nanoprojectile onto a rigid target initiates a complex sequence of events that results in a rapid build-up of stress and temperature and creation and energetic expulsion of fragment debris. The exploration of kinematic and thermal states in the highly-deformed nanoprojectile (including the debris cloud) and their mutual relationships is of considerable importance in many engineering fields. Various aspects of the propagation of stress and failure waves have been addressed in continuum mechanics and thermodynamics of shocks. Intrinsic instabilities in the thermo-mechanical deformation process at high-strain rates lead to localized deformation with profound effects on the dynamic response of materials on the macroscopic scale. Molecular dynamics (MD), performing the role of "a computational microscope," is an ideal tool to investigate deformation under extreme loading conditions by virtual testing.

The objective of the present article is twofold. First, to study nonuniform fragmentation of a monoatomic monocrystalline nanoscale projectile (nanoprojectile) subjected to the Taylor impact (rigid-anvil) test [1-3]. The second part of this work in progress is aiming at, perhaps elusive, goal to investigate temperature-related aspects of constitutive modeling *to be used* in the high-strain-rate mesoscale discrete simulations (such as [4,5]).

The Taylor test is established as a standard procedure to verify dynamic behavior of materials [3]. A series of two-dimensional (2D) MD simulations of this test is performed by using flat-ended nanoprojectiles made of the Lennard-Jones 6-12 (L-J) monocrystalline solid, matching, as close as possible, physical properties of tungsten ($_{74}$W). The three model parameters used are the atomic mass $m = 3.1 \times 10^{-25}$ kg (183.85 u), the atomic radius 1.4 Å ($\equiv r_0/2$ where r_0 is the equilibrium interatomic distance), and the depth of the potential well (the strength of the attraction) $\varepsilon_{LJ} = 7.5 \times 10^{-20}$ J estimated based on the sublimation energy [6]. The set of impact velocities covers the range from 0.75 km/s to the hypervelocity impact (7 km/s).

2. Technique of computer simulation

MD is a computer simulation technique frequently used to study evolution of discrete systems at spatial and temporal scales that go beyond the current experimental limits. The present investigation is limited to the traditional MD in which atomic interactions are defined by empirical potentials and atomic motions obey laws of classical mechanics [7]. Thus, in addition to structural information, the first important step in the MD simulations is definition of the interaction potential. In the present model, a monoatomic, monocrystalline system (mimicking a flat-nosed projectile) is comprised of atoms of known masses $m_i=m$ that form an ideal triangular lattice and interact with their nearest neighbors according to the L-J potential

$$\varphi(\bar{r}_{ij}) = -\varepsilon_{LJ} \left(2\bar{r}_{ij}^{-6} - \bar{r}_{ij}^{-12} \right), \quad \bar{r}_{ij} = (r/r_0)_{ij} \tag{1}$$

where $r_{ij} = |\boldsymbol{r}_j - \boldsymbol{r}_i|$ is the interatomic distance, $\boldsymbol{r}_i$ the position vector defining the location of ith atom, and subscript "0" marks the initial (equilibrium) interatomic distance in the reference configuration. The interatomic interactions are limited to the six nearest neighbors (the coordination number is six). In general, the nearest-neighbors approximation is due to two major reasons: (*i*) the electronic screening effectively limits the range of interatomic forces, and (*ii*) the long-range interactions are prohibitively computationally expensive for large systems. Although the L-J potential (1) is the most frequently used empirical potential for its simplicity, it should be noted that it cannot capture neither surface energy (stemming from imperfect coordination of the surface atoms) nor effects of the background electron density of surrounding atoms.

The dynamic state of the atomic system is defined by positions $\boldsymbol{r}_i$ and momenta $\boldsymbol{p}_i$ of N_{at} atoms constituting the nanoscale projectile, which can be derived from Newton's equation of motion rewritten in Hamiltonian form

$$\dot{\boldsymbol{r}}_i = \frac{\boldsymbol{p}_i}{m_i} = \frac{\partial \mathcal{H}}{\partial \boldsymbol{p}_i}, \quad \dot{\boldsymbol{p}}_i = -\frac{\partial V}{\partial \boldsymbol{r}_i} = -\frac{\partial \mathcal{H}}{\partial \boldsymbol{r}_i} \tag{2}$$

where a superposed dot denotes the material time derivative, $V(r_i)$ is the potential (defined by Eq. (1) in the present case) and

$$\mathcal{H}(\boldsymbol{r_i}, \boldsymbol{p_i}) = V(\boldsymbol{r_i}) + E_k(\boldsymbol{p_i}) = \sum_i V_1(\boldsymbol{r_i}) + \sum_i \sum_{j>i} V_2(\boldsymbol{r_i}, \boldsymbol{r_j}) + \sum_i \sum_{j>i} \sum_{k>j>i} V_3(\boldsymbol{r_i}, \boldsymbol{r_j}, \boldsymbol{r_k}) + \dots + \sum_i \frac{\boldsymbol{p_i^2}}{2m_i} \quad (3)$$

is Hamiltonian. (In the case of pairwise L-J potential $V(\boldsymbol{r_i}) \approx \sum_i \sum_{j>i} V_2(\boldsymbol{r_i}, \boldsymbol{r_j}) = \varphi(\bar{r}_{ik})$ of Eq. (1).)

The Cauchy problem definition is completed by a set of $4N_{at}$ initial conditions (2D)

$$\boldsymbol{r}(t=0) = \boldsymbol{r_0} \text{ and } \dot{\boldsymbol{r}}(t=0) = \dot{\boldsymbol{r}}_0 \quad (4)$$

and solved numerically by using the Verlet algorithm [7]

$$\boldsymbol{r_i}(t + \delta t) = 2\boldsymbol{r_i}(t) + \boldsymbol{r_i}(t - \delta t) + \frac{\delta t^2}{m} \sum_{j \neq i} \boldsymbol{f_{ij}}(\boldsymbol{r_i}, \boldsymbol{r_j}) \quad (5)$$

where δt is the time step and $\boldsymbol{f_{ij}} = -\nabla_i \varphi(r_{ik})$ is the force exerted by atom j on the atom i. For 2D L-J solid, the initial estimate of the time step is based on the expression

$$\delta t = \left(\frac{1}{60} \div \frac{1}{30} \right) \frac{2\pi}{\omega_E}, \quad \omega_E = \sqrt{3} \, \omega_0 \quad (6)$$

where ω_E is Einstein frequency defined in terms of the fundamental harmonic frequency $\omega_0 = C_0/r_0$ related to the sound speed and the equilibrium interatomic distance [11]. The time step obtained by Eq. (6) is of the order of femtoseconds.

Simulations generate information at the nanoscopic level: atomic positions and velocities, and interatomic forces. The conversion of this nanoscopic information to macroscopic observables such as temperature, stress and strain requires theories developed in the realm of statistical mechanics. Notably, the Boltzmann's ergodic hypothesis, which postulates that ensemble averages over the ensemble at a fixed time are equal to time averages over a single system.

The estimate of temperature evolution during extreme dynamic events, which is of crucial analytical importance, gives rise to some basic questions related to fundamental thermostatic concepts such as entropy and absolute temperature of a system that is far from equilibrium. As pointed out by Callen [8], the nonequilibrium entropy definitions are dependent on uncertain premises. Thus, a consensus appears to be established within the MD community over the last few decades that the most prudent approach is to use the Gibbs' temperature definition, familiar from the kinetic theory

$$k_B T = \left\langle \boldsymbol{p_i} \frac{\partial \mathcal{H}}{\partial \boldsymbol{p_i}} \right\rangle = \frac{1}{DN_x} \left\langle \sum_i \frac{\boldsymbol{p_i^2}}{2m_i} \right\rangle \quad (7)$$

which has the firm statistical-mechanics foundations since it follows from the canonical ensemble maximum-probability distribution [9]. In the preceding equation, D is the dimensionality of the

problem (e.g., D=3 in 3D), k_B the Boltzmann's constant, and N_x the number of atoms within the averaging area. Hoover and coworkers [10] argued that this standard temperature definition could be extended and applied to any stable configuration, even far from equilibrium. Indeed, it is claimed, "in nonequilibrium situations, the instantaneous kinetic temperature is the only meaningful definition" [11]. Therefore, the term "*temperature*," whenever used henceforth implies the "*instantaneous kinetic temperature*." Nonetheless, it should be kept in mind that "thermodynamic temperature ≡ long-time average of the instantaneous kinetic temperature at equilibrium" are the only rigorously defined equivalencies. Be it as it may, the temperature within an averaging area (2D: the unit thickness volume) centered on ith atom is defined as

$$ T_i = \frac{m}{2 N_i \, k_B} \sum_{j=1}^{N_i} \left(v_{xj}^2 + v_{yj}^2 \right), \quad \left(i = 1,...,N_{at} \right) \tag{8} $$

where N_i is the number of atoms of mass m belonging to the averaging area. Also, v_x and v_y are the vibrational velocity components (Figure 1) obtained by subtracting the velocity of correlative motion from the total particle velocity, $v_\alpha = v_{T\alpha} - \bar{v}_\alpha$, ($\alpha=x,y$). The total velocity, $v_{T\alpha}$, follows directly from the solution of Newton's equations of motion (2) while the velocity of correlative motion is obtained as the spatial average of total velocities of all atoms belonging to the averaging area $\bar{v} = \langle v \rangle$.
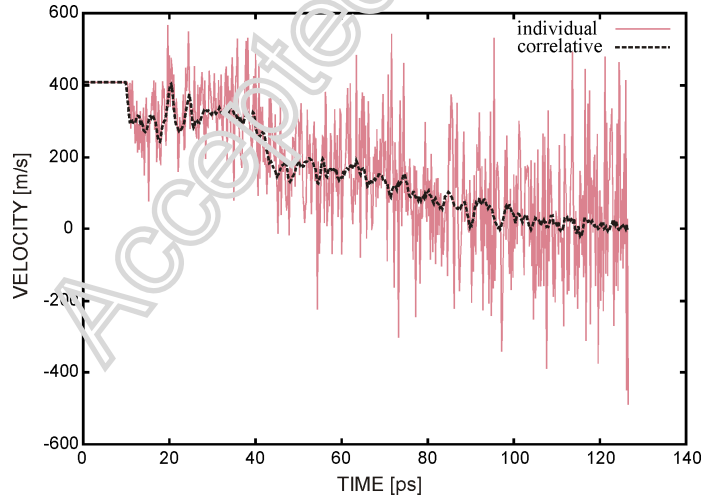

Figure 1. Time history of velocity in impact direction for striking speed of 0.408 km/s (1.2 Mach). The solid (pink) line and dashed (black) line represent the velocity of an individual atom and the corresponding velocity of correlative motion of group of atoms centred around that atom, respectively.

The instantaneous kinetic temperature (8) is averaged in both time (in accordance with the ergodic hypothesis) and space. The averaging area is commonly assumed to be the same circular region used for calculation of the velocity of correlative motion.

The statistical mechanics expressions for components of the mechanical stress tensor are

$$\sigma_{\alpha\beta} = \frac{1}{2\Omega} \sum_{\substack{i,j \\ i \neq j}} \frac{d\varphi(r_{ij})}{dr_{ij}} \frac{(r_{ij})_\alpha (r_{ij})_\beta}{|r_{ij}|} \tag{9}$$

where $(r_{ij})_\alpha$ is the α-component of the vector $\boldsymbol{r}_{ij}$, and Ω the sample "volume"; the alphabetic indices refer to particular atom, while the Greek letter subscripts are reserved for tensor components [14]. Zhou [15] demonstrated that the stress expression based on interatomic force term alone (9) is a valid mechanical stress measure at the scale of small set of atoms, which can be identified with the Cauchy stress. He indicated that the virial stress—the most commonly used definition of stress in discrete particle systems—cannot be regarded as a mechanical stress measure in any sence since the kinetic energy term leads to violation of balance of momentum (Zhou [15] and references therein).

The strain is calculated by comparing the lattice deviations in the current configuration from the reference configuration (the initial ideal lattice). Since the information about the atomic position is readily available in both current and the reference configuration, the calculation of the strain is straightforward. The components of the left Cauchy-Green strain tensor of ith atom in 2D systems are commonly defined by

$$b_{\alpha\beta} = \frac{1}{3} \sum_{j=1}^{6} (\bar{r}_{ij})_\alpha (\bar{r}_{ij})_\beta, \quad (\bar{r}_{ij})_\alpha = (r_{ij})_\alpha / r_0 \tag{10}$$

It should be noted that, unlike the stress counterpart (9), the virial strain (10) is valid instantaneously in time and space [16]. The nanoprojectile deformation at high impact velocities is characterized by extreme inelastic deformations followed by a substantial mass transfer via fragmentation; at the hypervelocity levels entire nanoprojectile is reduced to the fragment debris (Figure 2). Thus, rather than referring the length change of the original "gage" (10), it is more convenient to use the natural strain

$$\varepsilon(t) = \int_{L_0}^{L(t)} \frac{dL}{L} = \ln \frac{L(t)}{L_0} \tag{11}$$

for calculation of the longitudinal and lateral normal strains. In Eq. (11) the natural strain is defined in the usual manner as the change in dimension of a "virtual strain gage" ($L_0 \times L_0$) divided by the instantaneous value of the dimension.

3. Observations and discussion

The dynamic response of materials at high loading rates is inherently related to evolution of their microstructure. Defects at various scales, phase transformations, and their interplay govern the macroscopic behavior [12]. Some observations of dynamic response of the 2D L-J solid are presented below.

3.1. Distribution of fragment sizes

The kinetic energy E_{k0} of the projectile is during the impact partitioned among the excess kinetic and thermal energies of the fragments (and the projectile stump) and the fracture energy

$$E_{k0} = E_{k1} + E_d + E_f \qquad (12)$$

In Eq, (12), E_{k1} is the kinetic energy of the (rigid body) motion of the fragments upon the impact, E_d is the thermal energy associated with the thermal vibrations, and E_f is the randomly-distributed fracture energy dissipated in the process of fragmentation. Substantial literature exists in which the fundamental principles of dynamic fragmentation process were investigated both experimentally and theoretically [e.g., 3,13,23]. Because of inherent complexity, laboratory fragmentation tests are not able to "differentiate unambiguously among the various competing geometric statistical theories" [13]. Holian and Grady [13] were first to use MD to explore the fragmentation phenomena by simulating a homogeneous adiabatic expansion of condensed matter (aptly termed the microscopic "big bang"). Their results suggest that the cumulative distribution of fragment masses is well represented by the bimodal-exponential distribution and the average fragment mass can be explained by an energy balance between the kinetic energy of expansion and the potential energy of broken surface bonds. (According to Grady and Winfree [23] the cumulative exponential distribution follows from principles of classical statistical mechanics.)

One objective of the present set of simulations is to determine to what extent these results remain valid for a non-homogeneous (highly directional) fragmentation process caused by application of a *non-uniform* transient strain-rate field. The distribution of fragment sizes is studied, therefore, during the impact of a slender (53 × 429 atoms ≈ 15×110 nm), deformable L-J projectile with a rigid target. The results are presented in Table 1 and Figures 2 and 3.

Table 1. Cumulative frequency of fragment size N (in number of atoms constituting a fragment) at the end state for seven impact velocities. (Note that for the hypersonic impact velocities the nanoprojectiles are completely annihilated in the course of impact. In the other cases, the largest cluster corresponding to the arrested nanoprojectile is not included herein.)

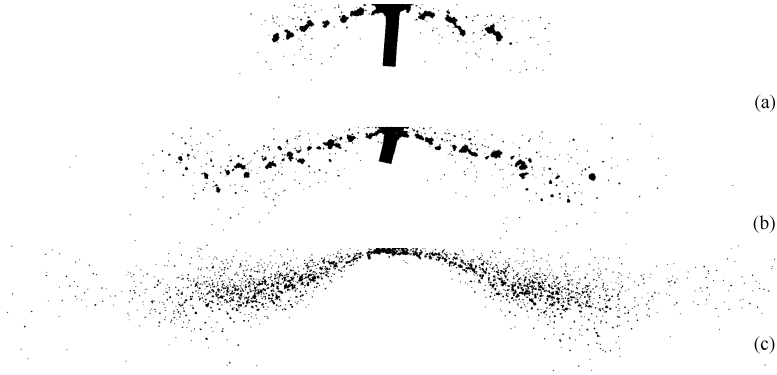|		v_i [km/s]				
		0.75	**1.0**	**2.0**	**3.0**	**4.0**
$\ln N = 0$	$N = 1$	1162	1603	3553	4178	3976
$0 < \ln N \leq 1$	$N = 2$	156	240	651	921	995
$1 < \ln N \leq 2$	$2 < N \leq 7$	93	171	584	824	842
$2 < \ln N \leq 3$	$7 < N \leq 20$	13	33	184	211	200
$3 < \ln N \leq 4$	$20 < N \leq 55$	6	16	49	63	51
$4 < \ln N \leq 5$	$55 < N \leq 148$	1	7	25	26	15
$5 < \ln N \leq 6$	$148 < N \leq 403$	1	1	13	9	3
$6 < \ln N \leq 7$	$403 < N \leq 1097$	1	7	3	2	2
$7 < \ln N \leq 8$	$1097 < N \leq 2980$	1	0	0	0	0

Figure 2. Fragmentation snapshots corresponding to the moment of the projectile arrest (a, b) or complete annihilation (c) for three impact velocities: (a) 0.75 km/s, (b) 1 km/s, and (c) 3 km/s. Note how the nanoprojectile at impact velocity approaching the hypervelocity impact threshold dissolves in a cloud of particles. For projectiles under high velocity impact it is of great importance to identify the fragmentation onset velocity defined as the threshold velocity just sufficient to completely shatter the projectile. For the present combination of the rigid target and the L-J monocrystalline solid, matching, as close as possible, physical properties of tungsten ($_{74}$W) the fragmentation onset velocity is just above 2 km/s, which agrees rather well with experimental observations.
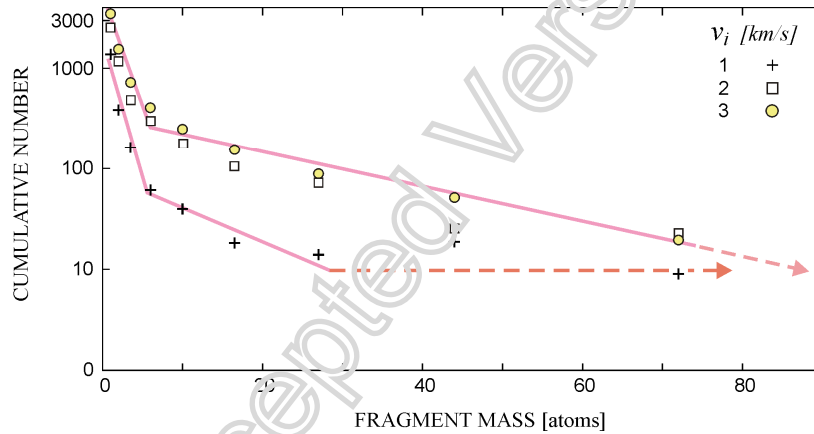

Figure. 3 Cluster statistics corresponding to the projectile arrest (1 km/s) or complete annihilation (3 km/s) in the course of the 2D Taylor test simulation. (Note that the mass of arrested projectile is not considered to be a fragment.)

The simulation results suggest that the bimodal-exponential distribution emerges in the smaller-clusters region for every impact velocity. For example, for $v_i = 0.75$ km/s the fragment size apparently obeys the bimodal-exponential distribution up to the range of 25-30 atoms (Figure 3), which implies that all larger fragments visible in Figure 2(a) are outside of it. This is not surprising bearing in mind that the bimodal-exponential distribution is obtained under the "big bang" simulation framework that largely precludes existence of relatively large fragments. The onset of the bimodal-exponential distribution breakdown increases with the impact-velocity increase since more energy becomes available for creation of new surfaces. Simulation results for $v_i = 2$ km/s indicate the fragment size corresponding to bimodal-exponential breakdown is approximately 50 atoms while for $v_i = 3$ km/s the breakdown seems to disappear, which might reflect the projectile annihilation illustrated by Figure 2(c). The later may be caused by the projectile's kinetic energy

7

sufficient to result in the adiabatic pulverization, similar to the Holian and Grady's "big bang" conditions [13]. More detailed investigation is effectively precluded by limitations of a relatively small MD model and our limited computational resources.

3.2. Temperature field

The high-strain-rate deformation is often adiabatic and the deformation work is transformed into heat with the attendant rise of temperature. As outlined by Meyers [3], this temperature increase has "a profound affect on the constitutive behaviour of the material because of the thermal softening, which may lead to shear instability." Intrinsic instabilities in the thermo-mechanical deformation process lead to localized deformation, which results in a nonuniform spatial distribution of thermal energy (Figure 4) and the corresponding fragment distribution strongly dependent on the imparted energy (Table 1). As a general premise, knowledge of the thermal history of a material deformed to extreme (Figure 5) should be useful in accessing parameters important for the mesoscale modeling.

A set of selected snapshots of temperature field evolution during the Taylor test at 1 km/s and 4 km/s are presented in Figure 4. These examples illustrate vividly the extreme temperature localization within a very narrow region of the contact zone. The simulation results demonstrate that since plastic deformation is localized to shear zones, the shear energy dissipated in the deformation process is also localized to these zones, resulting in large temperature gradients in the extremely deformed material. The obtained temperature distribution maps demonstrate that temperatures in the localized zones can be sufficient to cause melting even though the average temperatures may be below the melting temperature. The illustrations of the kind presented in Figure 4 indicate that the melting temperature of 3683 K [6] is reached in the contact zone even for relatively modest impact velocities such as 0.75 km/s (albeit into the rigid target), which is consistent with experimental evidence pointing to melting in the contact zone. The implication of this result on the computational terminal ballistics is far reaching from the standpoint of hydrodynamic theory (e.g., the selection of an appropriate friction coefficient in the contact zone for high-velocity impacts).

Examination of deformed configurations (such as those selected for Figure 4) reveals existence of vacancies, pores, and dislocations. These randomly distributed flaws are weak points in the contact-zone neighborhood at which the thermal softening and shear failure ultimately initiates. Although, these nanoscale heterogeneities may not be of interest *per se*, their effect can be averaged and characterized by a continuum description of the material response on a coarser scale [3]. The change of (crystalline) structure (suggesting phase transformations) can be noted as well, with the complete breakdown of initial crystalline regularity in the contact zone (Figure 4). The fragment

snapshots indicate nonequilibrium states since most clusters are far from spherical. It should be recalled that if a material undergoes a phase transformation, the linear equation of state (EOS) is no longer applicable [3]. The present simulation results indeed suggest a departure from linearity at the high impact velocities.
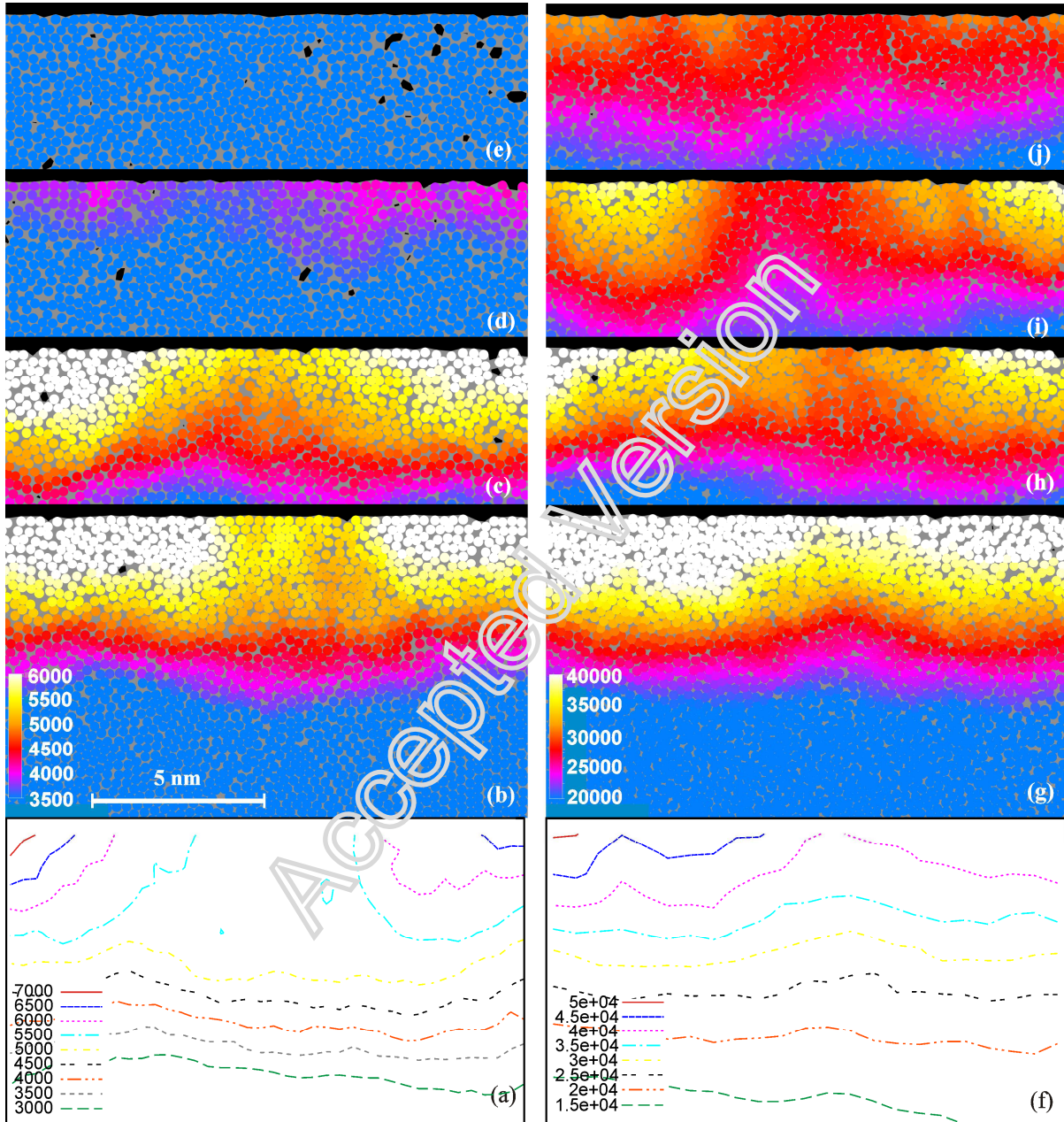

Figure. 4 Evolution of temperature [K] distribution in the contact region (aligned in the horizontal direction ±7.5 nm wrt. the projectile's centreline) during the Taylor impact tests with v_i = 1 km/s (the left side) and v_i = 4 km/s (the right side). The corresponding time histories of the selected state parameters are illustrated in Figure 5. The snapshots with individual atoms distinct correspond to the following time instances and number of fragments of various size: (a,b) 20 ps and 55, (c) 35 ps and 194, (d) 70 ps and 665, (e) 110 ps and 1337; (f.g) 7 ps and 566, (h) 10 ps and 1063, (i) 25 ps and 1958, (j) 20 ps and 2926. (Note an order of magnitude difference in the spatial thermal gradients.)

3.3. Scaling relations among macroscopic observables

Two sets of selected time histories of macroscopic observables (temperature, stress and strain invariant) are illustrated in Figure 5. The 2D state parameters presented are: the average normal stress, $P = (\sigma_x + \sigma_y)/2$; instantaneous kinetic temperature, T (8); and the effective strain defined herein as $\varepsilon_{eff} = \sqrt{(\varepsilon_x^2 + \varepsilon_y^2)/2}$.
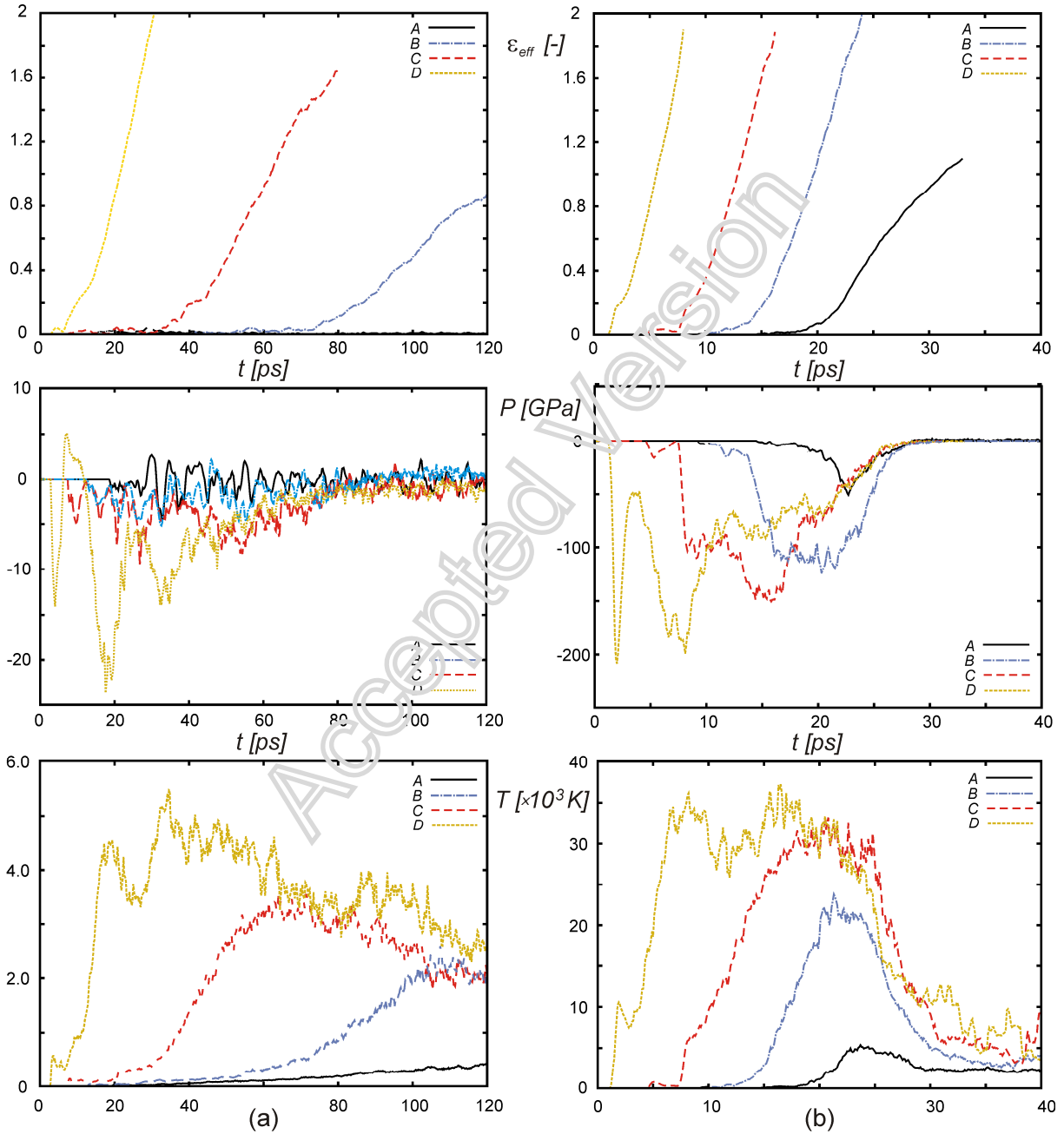

Figure. 5 Examples of time histories of state parameters recorded at four measurement areas equidistantly spaced along the projectile centerline from the distal (*A*) to the proximal end (*D*). Two selected impact velocities are: (a) 1 km/s, and (b) 4 km/s. Unlike in the case (a), the pressure time histories at 4 km/s start to reveal the familiar compression-wave features (note gages B and C).

The evolutions of the three state parameters are recorded at four measurement areas. The virtual "measurement gages", designated by capital alphabetical letters (*A-D*), are defined along the projectile's centerline equidistantly from the distal (*A*) to the proximal end (*D*, close to the flat nose) to mimic the strain and temperature measurement gages.

Table 2 presents the peak values of the selected state parameters recorded during the Taylor impact tests at seven striking velocities up to the hypervelocity impact (whose threshold is roughly in the range 3 to 4 km/s). It should be recognized that due to the target rigidity the impact velocities correspond to the contact-region particle velocity commonly encountered in shock physics. Due to the extreme character of the simulated events and the correspondingly ultrahigh peak values of the state parameters it is imperative to compare these values with the available high-velocity tests.

The peak "pressure" values recorded herein are of the same order of magnitude as the experimentally reported shock pressure for tungsten obtained, as an example, by Hixson and Fritz with two-stage light-gas gun [17]. These authors reported shock pressure of 263.88 GPa for the impact velocity of 4.514 km/s (the lowest they used). There are few reasons why the mean normal stress corresponding to $v_i = 4$ km/s in Table 2 falls below this experimental datum; three will be mentioned. Most importantly, the experiments were performed under the plain-strain (1D) conditions while the present 2D MD simulations of the Taylor test naturally exhibit lateral release waves and the lateral mass transfer. (In short, we are not modeling the experiment of reference [17]). Second, the L-J potential (1) used is an elementary pairwise potential that requires only two physical properties – one can expect only a limited quantitative agreement for a selected set of parameters with such simple atomic interaction model. Finally, the circular averaging area (mimicking measurement gages) is relatively large (with diameter $= 18 \, r_0$) and the proximal-end gage *D* is nearby but necessarily not exactly at the contact boundary (the highest-pressure region); this size of the averaging area is a result of a unavoidable compromise between the contradicting requirements for as large as possible size of the statistical sample and as small as possible resolution length of the calculation. All in all, the stress values obtained from the MD simulation appear to be in a reasonably good agreement with the experimental data, which is important to know before analyzing results for which only limited (or none whatsoever) experimental data is available.

While the peak pressures presented in Table 2 are commonly observed in shock-wave experiments, the peak temperatures (and consequently temperature rates given the rising times of few picoseconds) are rather puzzling.[1] The temperature results in Table 2 indicate not only that the

---

[1] Therefore, to get a sense of proportion it seems opportune to recall that temperatures of surface and core of the Sun are estimated to be 5800 K and 15×10^6 K, respectively; thermonuclear explosions are estimated to reach up to 1×10^8 K; nuclear fusion experiments 5×10^8 K. The experimentally verified temperature "of fast viscous heating of ions" recorded almost a decade ago at Sandia National Laboratories exceeded dumbfounding 2×10^9 K [22], which, amazingly enough,

melting temperature (3683 K) is reached in the contact zone at $v_i = 0.75$ km/s but the boiling temperature (5828 K) is probably reached in localized regions of the contact zone at impact velocities as low as $v_i = 1$ km/s. Critical point for tungsten is estimated by Rachel et al. [18] to correspond to $P_c = (1.1\pm0.2)$ GPa and $T_c = (16000\pm1000)$ K. With reference to Table 2, this implies that the fragmentation process during the hypervelocity Taylor test ($v_i > 3$-4 km/s) represents a transition to a homogeneous supercritical fluid ($P > P_c$ and $T > T_c$). Table 2 further indicates that even at $v_i = 1$ km/s the temperature rates exceed the those reported (~10^{13} K/s) for the electrically exploded Tungsten wires by Rakhel and Sarkisov [19]. The peak temperatures at the proximal end of the nanoprojectile (the measurement area D) exceed the melting temperature at all impact velocities presented in Table 2.

Table 2. The peak values of selected state parameters: pressure, temperature, temperature rate, strain rate, and acceleration of correlative motion for six impact velocities. and the acceleration of correlative motion ($\bar{a}$ corresponds to the velocity of correlative motion depicted schematically by the dashed line in Figure 1). The values are recorded at four measurement locations along the nanoprojectile centerline (with A and D corresponding to the distal and proximal end, respectively)

v [km/s]		0.75	1	2	3	4	5	7
P_{max} [GPa]	D	-12.	-23.	-62.	-140.	-195.	-270.	-540
	C	-5.0	-9.2	-47.	-90.	-150.	-245.	-480
	B	-4.0	-5.0	-28.	-70.	-125.	-210.	-440
	A	-2.0	-4.5	5.0	-20.	-50.	-65.	-180
T_{max} [$\times 10^3$ K]	D	3.7	5.4	15.5	24.5	38.0	58.5	109.
	C	2.7	3.5	9.4	17.5	32.5	43.0	90.0
	B	—	2.3	7.1	15.5	24.0	39.0	72.0
	A	—	—	2.0	2.5	5.5	9.0	18.0
$\dot{T}_{max}$ [$\times 10^{13}$ K/s]	D	8.0	34.3	150.	400.	800.	1500.	3050.
	C	5.8	11.5	90.	180.	350.	650.	1600.
	B	—	4.8	58.	150.	320.	670.	1550.
	A	—	—	15.	35.	130.	200.	1550.
$\dot{\varepsilon}_{eff}$ [$\times 10^9$ s^{-1}]	D	52.	102.	175.	265.	305.	400.	580.
	C	27.	47.	125.	191.	280.	325.	510.
	B	18.	21.	102.	175.	235.	310.	445.
	A	15.	—	46.	55.	104.	92.	190.
$\bar{a}$ [$\times 10^9$ km/s^2]	D	17.0	80.	210.	450.	740.	1000.	1850.
	C	11.5	27.5	130.	250.	390.	610.	1100.
	B	6.0	13.5	90.	230.	330.	620.	1100.
	A	6.0	9.0	50.	200.	320.	610.	1000.

Finally, the strain rates roughly estimated during the hypervelocity Taylor test reach $10^{11} \div 10^{12}$ s^{-1}. This strain rate range exceeds the strain rate "in excess of 10^{10} s^{-1}" obtained for *aluminum* by Crowhurst *et al.* [20], which appears to be the highest reported experimentally observed strain rate data. The hypervelocity "rigid-anvil" impacts exceed this range by two orders of magnitude due to the observed rise times of only a few picoseconds, Figure 5(b). Obviously, the

---

is not far away from the radiation temperature of the Universe approximately 1 second after the big bang, 1×10^{10} K (e.g., [25]).

dynamic behavior of materials subjected to the Taylor impact tests at supersonic striking velocities that reach such extreme strain rates in so minute time intervals are not accessible to diffusional processes [6,15].[2]

This part of the present investigation is aiming at temperature-related aspects of constitutive modeling to be used in the high-strain-rate mesoscale discrete simulations in which the thermal vibrations are not directly simulated (e.g., [7,8]). Analysis of the peak state properties recorded at various impact velocities (Table 2 and Figure 6) suggests the following scaling relation between the peak temperature and the strain rate

$$T_{\max} \propto \left(\dot{\varepsilon}_{eff}\right)^{5/3} \tag{13}$$

As illustrated in Figure 6, with impact velocity reduction below $v_i = 2$ *m/s* the scaling exponent *apparently* changes by approximately factor of three. It is not possible to extend this analysis further into the lower strain-rate regions under the present simulation setup since the lateral release waves prohibit formation of the smaller-intensity shocks under the Taylor-test loading conditions. A different simulations setup would be necessary to achieve this goal.
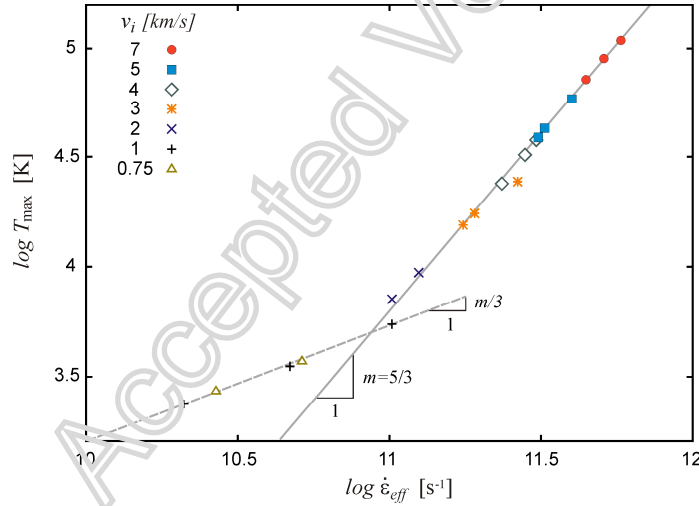

Figure. 6 Peak temperature dependence on strain rate recorded at three measurement areas (B-D) and seven impact velocities.

The results such as those selected for Table 2 also indicate fairly regular scaling relation

$$\dot{T}_{\max} \propto \left|\overline{a}\right|^{4/3} \tag{14}$$

between the peak temperature rate $\dot{T}_{\max}$ and the acceleration of the correlative motion $\left|\overline{a}\right|$ (Figure 6). It is important to note that the vibratory motions (the atomic scale phenomena related to

---

[2] It should be re-emphasized that the simulation results presented in Table 2 are obtained from a fairly small ($\approx$ 15×110 nm) and geometrically simple model for which boundary effects may be expected to become increasingly important for structural response. Perhaps it may be worthwhile to explore possibility to approach this extreme loading case from the standpoint of generalized higher-order continuum model with moving interfaces and energetic boundaries [24]. An alternative analytical approach to deal with nonlinear dynamical problems in a simplified manner is offered by the multiple time-scale method [26].

the instantaneous kinetic temperature by Eq. (8)) can be associated with the kinematic parameters (meso/macro scale properties) of the mesoscale discrete simulations, which potentially offers a natural way to introduce thermal effects at the mesoscale.
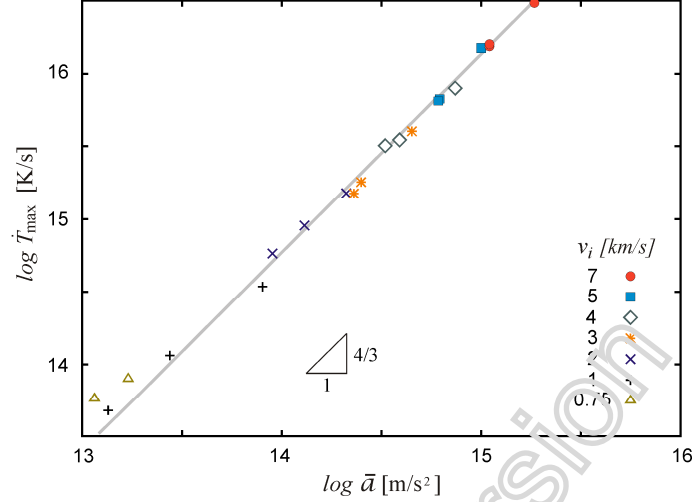

Figure. 7 Peak temperature-rate dependence on acceleration of correlative motion recorded at three measurement areas (B-D) and seven impact velocities.

3.4. Disturbance propagation velocity

For this set of simulations, the four measurement areas are positioned along the projectile's centreline close to the proximal end (the flat nose). The average velocity of disturbance propagation is defined herein as the ratio between the distance separating the first two measurement areas and the time lag between *compressive* stress pulse occurrences at the two locations. Simulations are performed for 16 impact velocities depicted in Figure 8. The dimensions of the plate-like projectile are 69×9 nm (247×59 atoms).
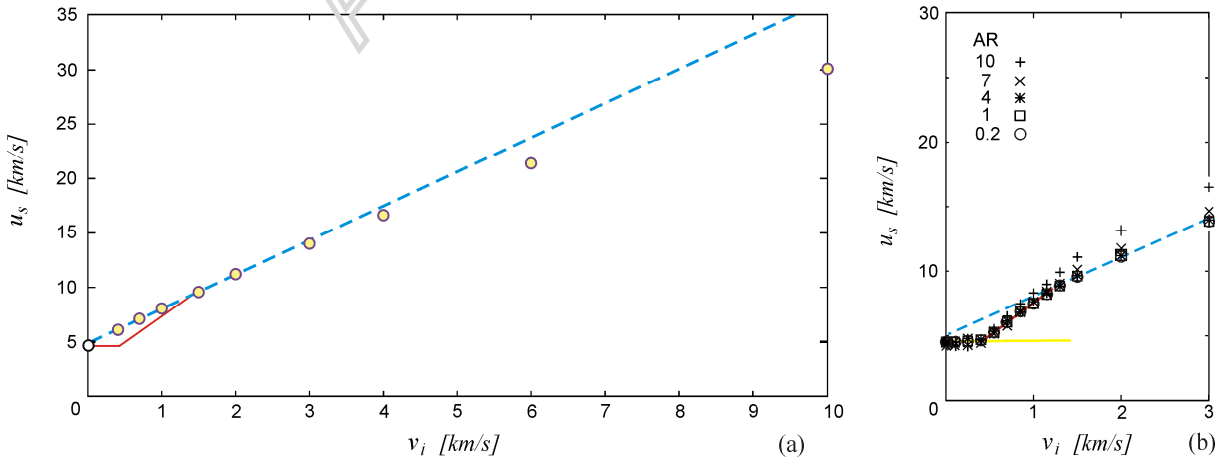

Figure. 8 Disturbance propagation velocity vs. impact velocity (a), and a detail revealing the effect of the attractive potential branch (initial transitory "pull") at low-velocities for five different aspect ratios of the nanoprojectile (b).

14

The simulation data plotted in Figure 8 suggest that the disturbance propagation velocity follows initially the linear form of EOS, $u_s = C_0 + S\, u_p$, which is common for most metals [3]. Here, u_s is the velocity of the shock front, u_p is the particle velocity (identified in the contact region with the impact velocity), C_0 is the sound velocity at zero pressure, and S is the empirical parameter (the slope of the shock Hugoniot). The velocity of longitudinal elastic wave propagation is within 5-10% of the reported values but the parameter S is not pinpointed that accurately [6,20]. More importantly, a steadily increasing departure from the initial linearity is observed in the hypervelocity range. This observation is consistent with the shock-induced phase transitions and in good agreement with experimental observations (e.g. [21]). Note the red solid line (Figure 8a) that shows schematically a peculiar small-scale phenomenon that occurs if the (minuscule) tensile ("pre-pull") stress pulse is accounted for at the smaller impact velocities (Figure 8b) due to the nature of the L-J interaction (1). The simulations are repeated for four projectiles of the same mass (thus, the same momentum and impact energy at a given v_i) but different aspect ratios (10, 7, 4, 1) to explore sensitivity of the results to the lateral confinement (Figure 8b).

4. Closure

Although the plasticity in small-sized crystalline metallic materials is extensively tested in the last few years, the similar experimental data is apparently not available at the high strain rates due to inherent experimental difficulties. Simulations of the Taylor test via molecular dynamics employed herein offer insights (admittedly rather limited due to the simplicity and small size of the model) into some thermo-mechanical aspects of nanoscale dynamic deformation at the extreme loading rates.

The bimodal-exponential distribution of fragment sizes that is observed during the uniform adiabatic expansion appears to hold for the hypervelocity impacts characterized by sufficiently high energy levels. The reduction of impact velocity during the non-uniform fragmentation, as expected, offers more complex fragment distributions that need to be further investigated. According to the simulation results, the cumulative distribution of fragment sizes, for more moderate impact velocities, in addition to the bimodal-exponential part, exhibits a large-fragment tail. Details of the cumulative fragment distribution, including the onset of the bimodal-exponential distribution "breakdown," are naturally highly dependent upon the impact energy. The breakdown threshold increases with increase of the impact velocity until it disappears at the hypervelocity level, which results in the bimodal-exponential distribution of fragments of a completely comminuted nano-projectile.

The time histories of the kinematic and thermal parameters of state are evaluated along the nanoprojectile. Their peak values obtained in the simulations (pressures approaching levels of TPa, temperatures of $\sim10^5$ K, and temperature rates in excess of 10^{15} K/s) reflect the extreme character of the loading. The observed scaling relationships between the mesoscale state parameters (the strain rate and the acceleration of correlative motion of particle groups) and temperature and temperature rate are promising steps toward the modelling of thermo-mechanical effects within the mesoscale discrete frameworks where atomic groups are lumped into "continuum particles."

Funding

References

[1] Taylor GE. The use of flat-ended projectiles for determining dynamic yield stress I. Theoretical considerations, *Proc Royal Soc London A* 1948; 194 (1038): 289–299.

[2] Wilkins ML and Guinan MW. Impact of cylinders on a rigid boundary. *J Appl Phys* 1973; 44: 1200-1207.

[3] Meyers MA. *Dynamic Behavior of Materials*. New York : John Wiley & Sons, 1994.

[4] Mastilovic S and Krajcinovic D. High-velocity expansion of a cavity within a brittle material, *J Mech Phys Solids* 1999; 47: 577–610.

[5] Mastilovic S. On strain-rate sensitivity and size effect of brittle solids: transition from cooperative phenomena to microcrack nucleation. *Continuum Mech Thermodyn* 2013. 25: 489–501.

[6] Weast RC. *Handbook of Chemistry and Physics*. Cleveland: CRC Press, 1976.

[7] Allen MP and Tildesley DJ. *Computer Simulation of Liquids*, Oxford: Oxford University Press, 1996.

[8] Callen HB. *Thermodynamics*, New York: John Wiley & Sons, 1961.

[9] Hoover WG. Canonical dynamics: Equilibrium phase space distributions. *Phys Rev A* 1985; 31: 1695-1697.

[10] Hoover WG, Holian BL and Posch HA. Comment on "Possible experiment to check the reality of a nonequilibrium temperature." *Phys Rev E* 1993; 48: 3196-3198.

[11] Holian BL, Voter AF and Ravelo R. Thermostatted molecular dynamics: how to avoid the Tada demon hidden in Nose-Hoover dynamics, *Phys Rev E* 1995; 52: 2338-2347.

[12] Bourne NK. Materials' Physics in Extremes: Akrology. *Metallurgical Mater Trans A* 2011; 42A: 2975-2984.

[13] Holian BL and Grady DE. Fragmentation by molecular dynamics: the micro-scopic "big bang". *Phys Rev Lett* 1988; 60: 1355-1358.

[14] Vitek V. Pair potentials in atomistic computer simulations. In: Voter AF (ed) *Interatomic potentials for atomistic simulations*, MRS Bulletin 21: 20-23, 1996.

[15] Zhou M. A new look at the atomic level virial stress: on continuum-molecular system equivalence. *Proc Royal Soc London A* 2003; 459: 2347-2392.

[16] Buehler MJ, Abraham FF, and Gao H.: Hyperelasticity governs dynamic fracture at a critical length scale. *Nature* 2003; 426: 141-146.

[17] Hixson RS and Fritz JN. Shock compression of tungsten and molybdenum. *J Appl Phys* 1992; 71(4): 1721-1728.

[18] Rakhel AD, Kloss A, and Hess H. On the Critical Point of Tungsten. *Int J Thermophys* 2002; 23(5): 1369-1380.

[19] Rakhel AD and Sarkisov GS. Melting and Volume Vaporization Kinetics Effects in Tungsten Wires at the Heating Rates of 10^{12} to 10^{13} K/s. *Int J Thermophys* 2004; 25(4): 1215-1233.

[20] Crowhurst JC, Armstrong MR, Knight KB, Zaug JM, Behymer EM. Invariance of the Dissipative Action at Ultrahigh Strain Rates Above the Strong Shock Threshold. *Phys Rev Lett* 2011; 107: 144302.

[21] Trunin RF, Medvedev AB, Funikov AI, Podurets MA, Simakov GV, and Sevast'yanov AG. Shock compression of porous iron, copper, and tungsten, and their equation of state in the terapascal pressure range. *Sov. Phys J Exp Theor Phys* 1989; 68(2): 356-361.

[22] Haines MG, LePell PD, Coverdale CA, Jones B, Deeney C, and Apruzese JP. Ion Viscous Heating in a Magnetohydrodynamically Unstable *Z* Pinch at Over 210 Kelvin. *Phys Rev Lett* 2006; 96: 075003.

[23] Grady DE, Winfree NA. Impact fragmentation of high-velocity compact projectiles on thin plates: A physical and statistical characterization of fragment debris. Int J Impact Engng 2001; 26: 249-262.

[24] Javili A, dell'Isola F and Steinmann P. Geometrically nonlinear higher-gradient elasticity with energetic boundaries. J Mech Phys Solids 2013; 61: 2381-2401.

[25] Allday J. *Quarks, Leptons and The Big Bang*. Bristol: IOP Publishing, 2001.

[26] Luongo A, Paolone A. On the Reconstitution Problem in the Multiple Time-Scale Method. Nonlinear Dynamics 1999; 19: 133-156.